

Supplementary Information for

**Dual-point noncoaxial rotational Doppler effect towards
synthetic OAM light fields for real-time rotating axis detection**

Yanxiang Zhang¹, Zijing Zhang^{1,*}, Han Lin³, Zhongquan Nie^{2,*}, Rui Feng¹, Yuan Zhao¹, and
Baohua Jia^{3,*}

¹School of Physics, Harbin Institute of Technology, Harbin 150001, China

²Key Lab of Advanced Transducers and Intelligent Control System, Ministry of Education and
Shanxi Province, College of Electronic Information and Optical Engineering, Taiyuan University of
Technology, Taiyuan 030024, China

³Centre for Atomaterials and Nanomanufacturing (CAN), School of Science, RMIT University,
Melbourne, 3000 VIC, Australia

This PDF file includes:

Supplementary Notes 1-8

Supplementary Figures 1-8

Supplementary Notes 1: Creation and characterization of synthetic OAM light fields

To achieve real-time, high-energy efficiency and high-accuracy detection in rotating axis orientations, it is necessary to create customized OAM light fields with four-hotspots that meet the orthogonality and rotational symmetry requirements. Towards this end, we adopt to a linear strategy that involves coherently superposing $N(N > 1)$ pairs of specific phase-conjugated OAM light fields. This process can be formulized in the cylindrical coordinates (r, φ, z) at $z = 0$:

$$E_N(r, \varphi) = \sum_{n=1}^N E_{p, \pm l_n}(r, \varphi) \quad (\text{S1})$$

with the conjugate superposed OAM light fields:

$$E_{p, \pm l_n}(r, \varphi) = E(r) [\exp(il_n\varphi) + \exp(-il_n\varphi)] \quad (\text{S2})$$

where the radial-related complex amplitude,

$$E(r) = E_0 \left(\frac{\sqrt{2}r}{\omega_0} \right)^{|l_n|} L_p^{|l_n|} \left(\frac{2r^2}{\omega_0^2} \right) \exp\left(-\frac{r^2}{\omega_0^2}\right) \quad (\text{S3})$$

in which E_0 is the amplitude factor. ω_0 is the beam waist of the Gaussian beam. $L_p^{|l_n|}$ is the Laguerre polynomial with radial mode index $p = 0$. More importantly, the OAM index l_n plays a pivotal role in our study. They can be constructed by using either an arithmetic sequence with the first term and common difference both being 4, or a geometric sequence with the first term of 4 and the common ratio of 2. Specifically, $l_n = 4n$ or $l_n = 2^{n+1}$ for a n -th superposed phase-conjugated OAM light field. The corresponding customized OAM light fields can also be classified as either arithmetic sequence E_N^{as} or geometric sequence E_N^{gs} . The simulated light field distributions for both two cases are shown in Fig. S1, respectively. As we can see from Fig. S1, assigning each of the two different sets of OAM indices l_n to the superposed phase-conjugated OAM light fields can create four-hotspots OAM light fields.

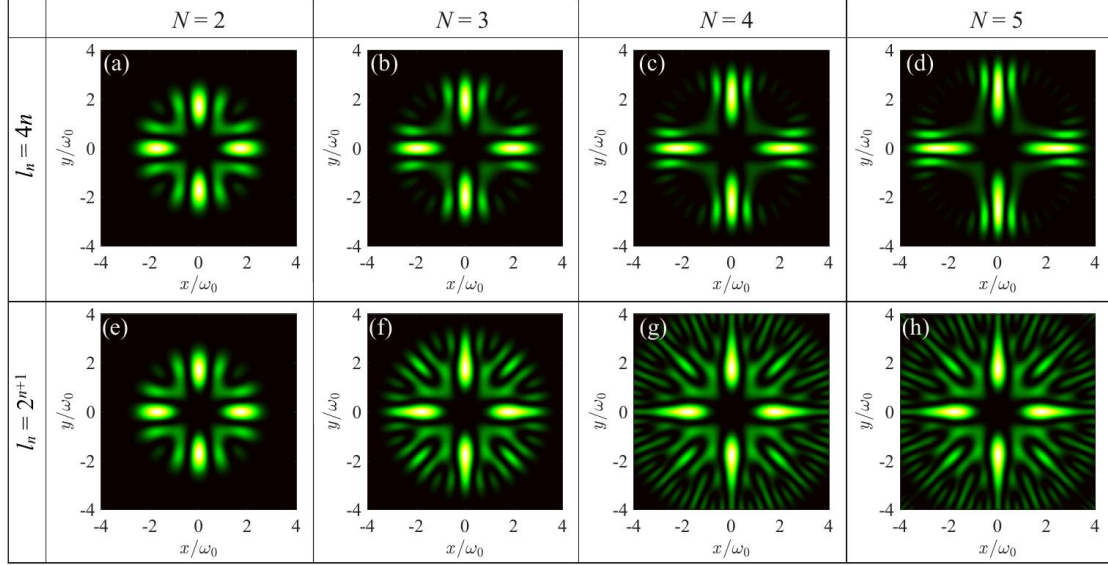


Figure S1 The distributions of partial synthetic OAM light fields with four main hotspots. The four-hotspots OAM light fields generated by (a) $E_2^{as} = E_{0,\pm 4} + E_{0,\pm 8}$; (b) $E_3^{as} = E_{0,\pm 4} + E_{0,\pm 8} + E_{0,\pm 12}$; (c) $E_4^{as} = E_{0,\pm 4} + E_{0,\pm 8} + E_{0,\pm 12} + E_{0,\pm 16}$; (d) $E_5^{as} = E_{0,\pm 4} + E_{0,\pm 8} + E_{0,\pm 12} + E_{0,\pm 16} + E_{0,\pm 20}$ with OAM indices of the arithmetic sequence $l_n = 4n$. The four-hotspots OAM light field distributions created by (e) $E_2^{gs} = E_{0,\pm 4} + E_{0,\pm 8}$; (f) $E_3^{gs} = E_{0,\pm 4} + E_{0,\pm 8} + E_{0,\pm 16}$; (g) $E_4^{gs} = E_{0,\pm 4} + E_{0,\pm 8} + E_{0,\pm 16} + E_{0,\pm 32}$; (h) $E_5^{gs} = E_{0,\pm 4} + E_{0,\pm 8} + E_{0,\pm 16} + E_{0,\pm 32} + E_{0,\pm 64}$ with OAM indices of the geometric sequence $l_n = 2^{n+1}$.

Furthermore, it is worth to mention that the quality of the synthetic OAM light is important for the probing rotating axis orientations. It is well-known that any complex-valued functions can be represented as the superposition of a set of orthogonal complete basis vectors. Laguerre-Gaussian modes ($LG_{p,l}$) within Hilbert space is a set of orthogonal and complete basis vectors and any optical fields can be superposed by them [S1, S2], with no exception to the synthetic OAM light fields E_N . Mathematically, this superposition process can be formulized as:

$$E_N(r, \varphi, z) = \sum_{p,l} A_{p,l} LG_{p,l}(r, \varphi, z) \quad (\text{S4})$$

where $A_{p,l}$, with radial index $p = 0$, characters the weighting of each basis vector within the synthetic OAM light fields, and its intensity denotes the OAM spectrum which can be described by following inner product operation as:

$$|A_{p,l}|^2 = \left| \iint LG_{p,l}^*(r, \varphi, z) E_N(r, \varphi, z) r dr d\varphi \right|^2 \quad (\text{S5})$$

According to Eqs. (S4), (S5) and Eq. (1) in the main manuscript, we thus simulate the on-axis OAM spectra of synthetic OAM light fields E_N with $N = 2, 3, 4, 5$, as shown in Fig. S2. As we can see, the $-8, -4, +4$ and $+8$ -order intramodal components possess totally parallel weightings in E_2 fields (see Figs. S2(a) and S2(b)). This is because E_2 fields consist of these four equal-proportional mode components given by Eq. (1) in the main manuscript. The same law can also be compatible with E_3 fields in Figs. S2 (b) and (f) as well as E_4^{as} fields in Fig. S2 (c). Whereas Figs. S2(d), (g) and (h) shows the weighting mismatches between the intramodal components, especially for high-order intramodal components, owing to there exist the salient discrepancies for the modal radius of high-order projecting modes with the synthetic OAM light fields. Nonetheless, in practice, we can manipulate the radii of uploaded projecting modes with a well-established diffractive optical element, and thus this would indeed have no impact on our final detection results.

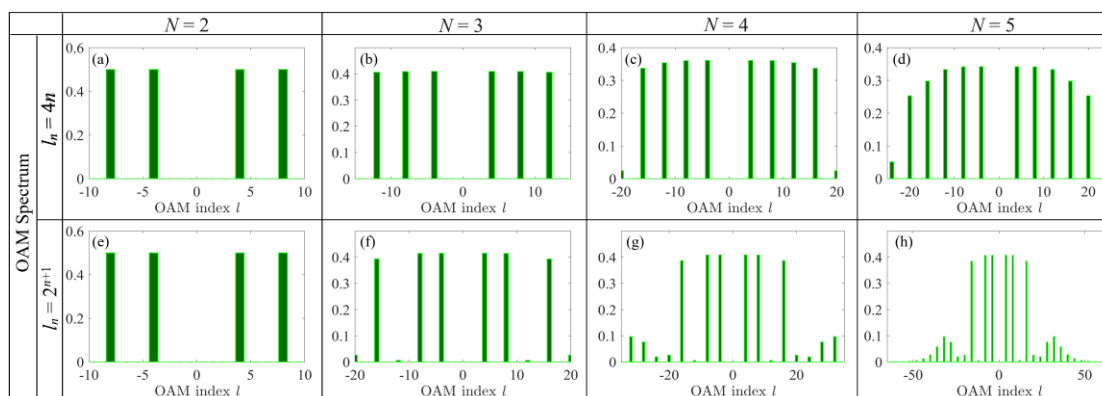


Figure S2 Characterization of quality of synthetic OAM light fields with OAM spectrum. The OAM spectra corresponding to synthetic OAM light fields generated by (a) $E_2^{as} = E_{0,\pm 4} + E_{0,\pm 8}$; (b) $E_3^{as} = E_{0,\pm 4} + E_{0,\pm 8} + E_{0,\pm 12}$; (c) $E_4^{as} = E_{0,\pm 4} + E_{0,\pm 8} + E_{0,\pm 12} + E_{0,\pm 16}$; (d) $E_5^{as} = E_{0,\pm 4} + E_{0,\pm 8} + E_{0,\pm 12} + E_{0,\pm 16} + E_{0,\pm 20}$ with OAM indices of the arithmetic sequence $l_n = 4n$. The OAM spectra matching synthetic OAM light fields created by (e) $E_2^{gs} = E_{0,\pm 4} + E_{0,\pm 8}$; (f) $E_3^{gs} = E_{0,\pm 4} + E_{0,\pm 8} + E_{0,\pm 16}$; (g) $E_4^{gs} = E_{0,\pm 4} + E_{0,\pm 8} + E_{0,\pm 16} + E_{0,\pm 32}$; (h) $E_5^{gs} = E_{0,\pm 4} + E_{0,\pm 8} + E_{0,\pm 16} + E_{0,\pm 32} + E_{0,\pm 64}$ with OAM indices of the geometric sequence $l_n = 2^{n+1}$.

Supplementary Notes 2: DNRDE induced by synthetic OAM light fields

In mathematical picture, we first establish a fixed Cartesian coordinate system with the

light field's center O as the origin and the four hotspots at x - and y -axes, respectively. For the first point P1, as shown in Figs. 1 and 2(e) in the main text, the noncoaxial RDSs can be obtained using the principle of linear Doppler effect due to a shared origin [S3]:

$$f_{RDE-1}^{l_n} = \frac{f_0 |\vec{v}_1| \cos \tau_1 \sin \beta}{c} \quad (S6)$$

where $f_0 = c / \lambda$ is the light frequency with the light speed c . $|\vec{v}_1| = \Omega |\vec{R}_1|$ is the linear velocity of the point P1, in which $|\vec{R}_1|$ stands for the rotating radius of P1 versus rotating axis O' , and β denotes the skew angle of the Poynting vector with respect to light axis, which is written as $\beta = l_n \lambda / 2\pi |\vec{r}_1|$ [1, S4, S5]. $\cos \tau_1$ shown in Fig. 2(e) can be represented with vector \vec{R}_1 and vector \vec{r}_1 through an angle transform:

$$\cos \tau_1 = \frac{\vec{R}_1 \cdot \vec{r}_1}{|\vec{R}_1| |\vec{r}_1|} \quad (S7)$$

As a result, Eq. (S4) can be rewritten as:

$$f_{RDE-1}^{l_n} = \frac{l_n \Omega (\vec{R}_1 \cdot \vec{r}_1)}{2\pi r_1^2} \quad (S8)$$

Given the point coordinates $O(0,0)$, $P1(r_1,0)$, and $O'(d \cos \gamma, d \sin \gamma)$, we can obtain the distance vector: $\vec{r}_1 = \overrightarrow{OP1} = (r_1, 0)$, $\vec{d} = \overrightarrow{OO'} = (d \cos \gamma, d \sin \gamma)$, $\vec{R}_1 = \overrightarrow{O'P1} = \vec{r}_1 - \vec{d} = (r_1 - d \cos \gamma, -d \sin \gamma)$. Hence, $\vec{R}_1 \cdot \vec{r}_1 = r_1(r_1 - d \cos \gamma)$. Consequently, the noncoaxial RDS at the point P1 can be manifested as the following form:

$$f_{RDE-1}^{l_n} = \frac{l_n \Omega (r_1 - d \cos \gamma)}{2\pi r_1} \quad (S9)$$

Similarly, for the point P2, we can also garner the noncoaxial RDS as:

$$f_{RDE-2}^{l_n} = \frac{l_n \Omega (r_2 - d \sin \gamma)}{2\pi r_2} \quad (S10)$$

It is worth noting that Eqs. (S7) and (S8) describe the DNRDE induced by a single OAM mode l_n . To obtain the detectable RDE, the magnitudes of these shifts can be doubled by taking into account the beating effect between conjugated OAM light modes

of $\pm l_n$. As a consequence, assuming that the distances from P1 and P2 to the origin are the same, denoted by $r_1 = r_2 = r$, the dual-point noncoaxial RDE of the customized OAM light field at these two points can be expressed as follows:

$$f_{RDE-1} = \frac{|l_n| \Omega (r - d \cos \gamma)}{\pi r} \quad (\text{S11})$$

$$f_{RDE-2} = \frac{|l_n| \Omega (r - d \sin \gamma)}{\pi r} \quad (\text{S12})$$

Supplementary Note 3: Experimental setup for the generation of synthetic OAM light fields and real-time detection of rotating axis orientations

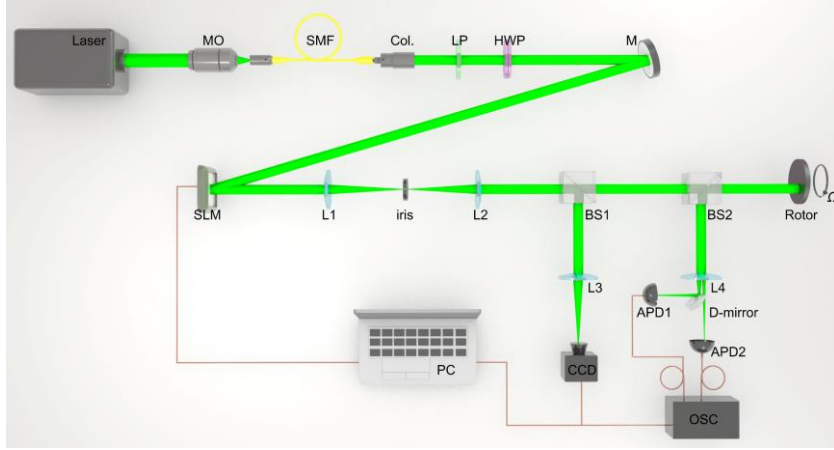


Figure S3 Experimental setup. MO: micro-objective; SMF: single-mode fiber; Col: collimator; LP: linear polarizer; HWP: half wave plate; M: mirror; SLM: spatial light modulator; L3: lens; L4: micro-lens array; BS: beam splitter; CCD: charge coupled device; APD: avalanche photodetector; OSC: Oscilloscope; PC: personal computer.

Supplementary Notes 4: Experimental generation of synthetic OAM light fields E_2

In experiment, we here select the customized OAM light field E_2 as the emitted light field to detect the orientations of rotating axes. As illustrated in Eq. 1 and Fig. 2, the generation of E_2 requires superposing ± 4 -order and ± 8 -order OAM light fields. In our experiment, we use a versatile complex-amplitude-modulated technique to encode E_2 as the computer-generated hologram, which is then loaded onto the SLM. This

enables us to experimentally produce the emitted light field. In Fig. S4, we show the encoded holograms (Figs. S4(a)-(c)), the generated OAM light fields (see Figs. S4 (d) and (e)) as well as the customized OAM light field (see Fig. S4 (f)), respectively. As displayed, the experimental results are basically consistent with that of numerical simulations. It is worth noting that there is a salient difference between the experimental and simulated results for E_2 in Figs. 2(c) and S4 (f): the presence of the sidelobes sandwiched between four hotspots. However, we are able to effectively eliminate these side lobes using an energy threshold approach. Specifically, we set a threshold for the energy of the light field, and any values below this threshold are set to null, while that exceeding the threshold are maintained at a constant level. Here, we choose a threshold value of 40% of the maximum normalized energy of the light field, which is the experimental criticality for the presence/absence of sidelobes. Since we are only interested in the information carried by the main lobes, such eliminations have no impact on the eventual detection results of rotating axis orientations.

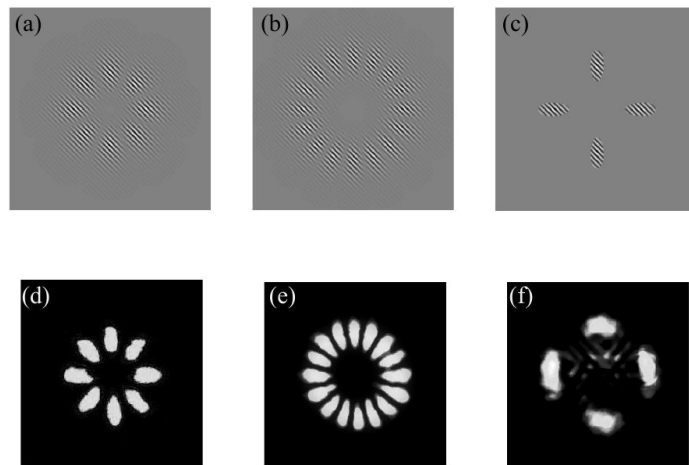


Figure S4 The loaded holograms on the SLM and experimentally produced light fields for (a) and (d): ± 4 -order light field; (b) and (e): ± 8 -order light field as well as (c) and (f): customized OAM light field E_2 .

Supplementary Notes 5: Signal post-processing

Here, we perform the signal post-processing on the Doppler signals to remove noise

and smooth the data, by exploiting the spectral subtraction (SS) method [S6] and a designed Wiener filter (WF). We provide a schematic diagram of this processing in Fig. S5. Specifically, the pose-processing involves representing the noisy signal $y(n)$ as the sum of a clear signal $x(n)$ and an additive noise $n(n)$, which allows for the extraction of the clear signal and removal of the noise:

$$y(n) = x(n) + n(n) \quad (\text{S13})$$

where, n stands for time index. Our goal using the SS method is to obtain the power spectrum of the clear signal $x(n)$. To achieve this, we transform the temporal signals in Eq. S11 from time domain into frequency domain via the discrete Fourier transform (DFT). Since the SS method works on segmented data, we need to divide $y(n)$ into K equal data chunks using a window function (e.g., a hamming window). The noise $n(n)$ can be actively selected from the segmented data. After calculation, the transformed noisy signal within the frequency domain can be given by:

$$Y_k(\omega) = X_k(\omega) + N_k(\omega) \quad (\text{S14})$$

in which k denotes the k -th data point in the data chunks. As a result, the power spectrum of clear signal can be manifested through power SS technology, as:

$$|\hat{X}_k(\omega)|^2 = |Y_k(\omega)|^2 - a \overline{|N_k(\omega)|^2} \quad (\text{S15})$$

Here, $|\hat{X}_k(\omega)|^2$ and $|Y_k(\omega)|^2$ are estimated power spectrum and the power spectrum

of the noisy signal, respectively. $\overline{|N_k(\omega)|^2} = \sum_{k=0}^{K-1} |N_k(\omega)|^2 / K$ denotes time-averaged

power spectrum of the noise $n(n)$. The scaling factor of a defines the magnitude of noise subtraction. After implementing the power SS according to Eq. S13, multiple negative values might arise in the estimated power spectrum, which does not be practical. As such, another parameter of b , named noise floor, can be introduced to convert the negative values into useful positive values. Such that Eq. S6 can be rewritten with the noise floor as:

$$|\hat{X}_k(\omega)|^2 = \begin{cases} b \overline{|N_k(\omega)|^2}, & \text{if } |\hat{X}_k(\omega)|^2 < b \overline{|N_k(\omega)|^2} \\ |Y_k(\omega)|^2 - a \overline{|N_k(\omega)|^2}, & \text{otherwise} \end{cases} \quad (\text{S16})$$

The introduction of the scaling factor a and the noise floor b can effectively improve the signal quality by achieving de-noising and the smoothing of estimated power spectrum. Noting that we here choose $a=4$ and $b=1\%$ to carry out the power SS.

In practical signal post-processing, this estimated power spectrum is a $K \times (L-1)$ matrix (L is the sample length) as the functions of time and frequency due to the segmented data used, which is not convenient for the comparison with the prescribed frequency threshold. To display the estimated power spectrum as a function of frequency, we first combine the estimated power spectrum with the phase spectrum $\phi_Y(\omega)$ of noisy signal to reconstruct the estimated time signal $\hat{x}(n)$, and then we perform the inverse DFT. Afterwards, we design a WF using the power spectra of the noisy signal and estimated power spectrum of the clear signal:

$$H(\omega) = \frac{|\hat{X}_k(\omega)|^2}{|Y_k(\omega)|^2} \quad (\text{S17})$$

As a result, the estimated amplitude spectrum $X(\omega)$ of the signal $\hat{x}(n)$ can be filtered using the convolution with this filter applied to the amplitude spectrum $Y(\omega)$ of the noisy signal. Then, the estimated power spectrum can be obtained by the operating norm of $X(\omega)$.

$$|X(\omega)|^2 = |H(\omega) * Y(\omega)|^2 \quad (\text{S18})$$

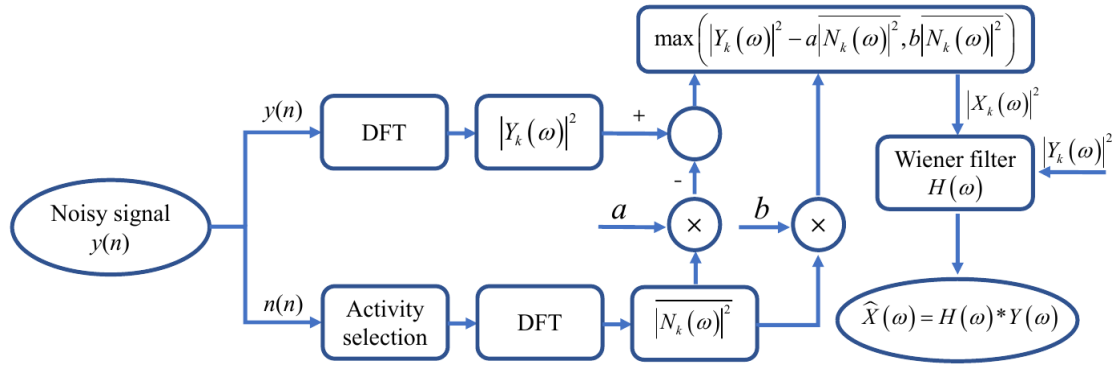


Figure S5 The schematic of signal post-processing. This processing can be achieved by the SS method and a designed Wiener filter.

Supplementary Notes 6: Performance analyses (measurement sensitivity, range, resolution, and precision) and the influence of synthetic OAM light fields on these performance indicators

Note that the quantitative performance analyses including measurement sensitivity, range, resolution, and precision are important for practical applications. As such, we respectively formulize and analyze these performance indicators for detecting rotating axis orientations as follows:

(1) First of all, the measurement sensitivity can be quantified as the minimum detectable power P_{min} on the detectors when the signal-to-noise ratio (SNR) equals approximately to one. The SNR can be defined as the ratio of the maximum signal peak (S_{max}) to the maximum noise peak (N_{max}) within detectable frequency bandwidth range, which can be described as:

$$\text{SNR} = \frac{S_{max}}{N_{max}} \quad (\text{S19})$$

These two peak values can be found in the Doppler power spectrum shown on the oscilloscope display screen. At this time, the received power can be detected by a power meter. After multiple measurements (~ 20 times), the statistical power value can be recognized as the final result, which characterizes the system sensitivity. For this point, we use the synthetic OAM field field of E_2 as an example for illustration, and then we measure the minimum detectable power P_{min} at the detection end, which is roughly $0.63 \mu\text{W}$ under our experimental conditions.

(2) As a proof-of-principle experiment, the detectable distance is currently restricted into the laboratory area range ~ 4 m. However, the detectable distance in practical applications can be significantly extended. Theoretically, the minimum detectable distance can be determined by the Rayleigh range when considering the propagation divergence case. As an example, the synthetic OAM light fields E_2 give the Rayleigh range approximately represented as $z_R = kr^2 / 2 = \pi r^2 / \lambda$, where $r \approx 2.5$ mm being the radius of the beam waist of E_2 measured by a beam profiler, and $\lambda = 532$ nm representing the wavelength of the light field. As a result, the minimum detectable distance can be calculated as: $z_R = \pi \times (2.5 \times 10^{-3})^2 / (532 \times 10^{-9}) \approx 36.9$ m. In more practical cases, this detectable distance can be further extended to a few kilometers when using existing single-photon detection technology [S7, S8].

(3) The rotating axis is determined by the measured dual-point noncoaxial rotational Doppler shifts, and hence its resolution depends on the frequency resolution Δf within the Doppler spectrum. The frequency resolution within the frequency domain Δf rests with sampled time length T data within the temporal domain following $\Delta f = 1/T$. The sampled time length $T = 0.1$ s throughout our experiments, and thus the frequency resolution is 10 Hz. As a consequence, the resolution of the measured rotating axis orientations can be estimated with Eqs. (2) and (3) in the main manuscript under certain experimental conditions. After calculation, the resolution of rotating axis orientations is roughly 5.42° .

(4) In our original manuscript, we define the measurement precision of the rotating axis orientations by the absolute measurement error, i.e., the absolute value between theoretical and measured values:

$$\eta = |\gamma_{th} - \gamma_{measured}| \quad (\text{S20})$$

It is worth to mention that the smaller the absolute error, the higher the measurement precision, vice versa. As shown in Fig. 6(e) in the main manuscript, the measured maximum absolute error is less than 2.23° within full orientation range after implementing the statistical measurement.

In addition, in order to illustrate the influence of synthetic OAM light fields on these

performance indicators (i.e., sensitivity, distance, resolution and precision), we measure the minimum detectable power P_{min} , detection distance z , frequency resolution Δf and measurement absolute error η when emitting synthetic OAM light fields E_2 , E_3^{as} , E_4^{as} , E_5^{as} and E_5^{gs} corresponding to optical modal filters ± 8 , ± 12 , ± 16 , ± 20 , ± 32 , respectively. Here, the superscripts of ‘as’ and ‘gs’ denote the arithmetic and geometric sequences, respectively, corresponding to the first and the last rows in Fig. S1. The measured emitted light fields and uploaded optical modal filters on SLM1 and SLM2 are shown in Fig. S6, respectively, and the corresponding measured results are illustrated in Fig. S7. Figure S7(a) shows that the minimum detectable power P_{min} displays a slightly increased trend with the synthetic OAM light fields and uploaded optical modal filters. This might be due to that the uploaded high-order modal filter leads to the larger dual-point Doppler frequency shifts according to Eqs. (2) and (3) in the main manuscript, thereby moving the signal peak away from the low-frequency noise domain. This further enhances the SNR, and hence improves the sensitivity of the system. In Fig. S7(b), it shows that all the detectable distances can be up to 4 meters in our laboratory area conditions (6.5m×5m×3.3m) when altering the emitted light fields and modal filters. And thus, the detectable distance within laboratory conditions has nothing to do with the synthetic OAM light fields. Since the frequency resolution Δf is dominated by the sample time length T , the synthetic OAM light fields have no impact on the resolution of measured rotating axis orientations, as shown in Fig. S7(c). Moreover, we measure the rotating axes within full orientations according to Fig. 6(e) when varying the synthetic OAM light fields and optical modal filters. The corresponding maximum absolute errors η are shown in Fig. S7(d). We can see that the measured errors almost maintain constant. This can be understood that when SNR within the Doppler spectrum is larger than 1, the measured accuracy is just determined by frequency resolution, rotation motor stability and the distance between rotating and light axes, whereas if the SNR is less than 1, the signal is submerged into noises making the measurement system disabled, thereby leading to larger errors and lower precisions. In these situations of Fig. S7(d), all SNRs are larger than 1, and the variations of

synthetic OAM light fields are insensitive to the measurement precision.

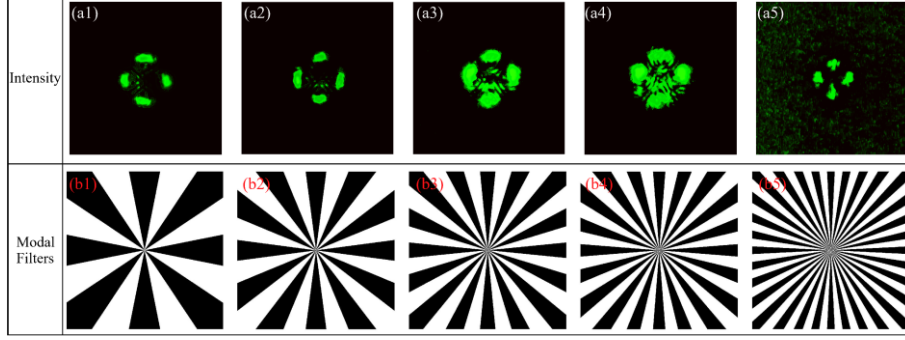


Figure S6 The measured light field distributions of (a1) E_2 ; (a2) E_3^{as} ; (a3) E_4^{as} ; (a4) E_5^{as} ; (a5) E_5^{gs} as well as corresponding optical modal filters of (b1) ± 8 ; (b2) ± 12 ; (b3) ± 16 ; (b4) ± 20 ; (b5) ± 32 uploaded on SLM1 and SLM2, respectively.

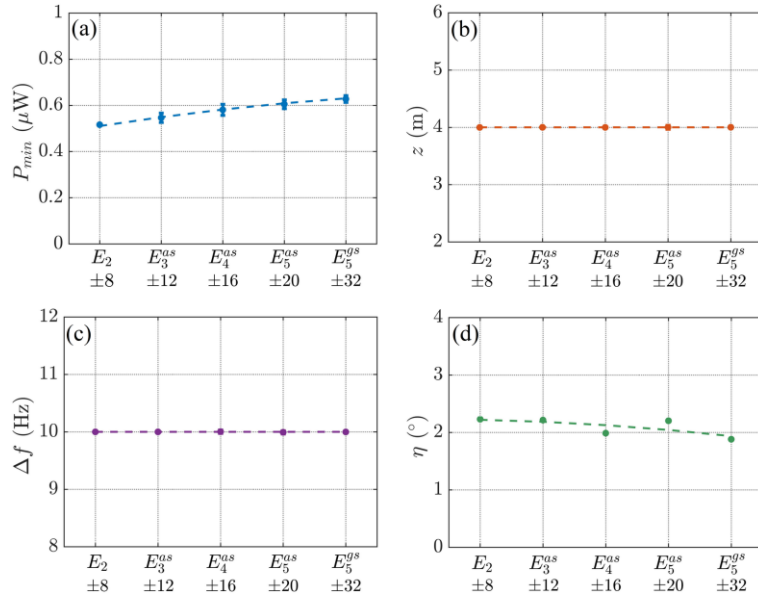


Figure S7 The dependences of system performance on synthetic OAM light fields. (a) The minimum detectable power P_{min} , (b) distance z , (c) frequency resolution Δf and (d) maximum absolute error η when emitting synthetic OAM light fields (the labels of the first row on the horizontal axis) of E_2 , E_3^{as} , E_4^{as} , E_5^{as} and E_5^{gs} as well as uploading optical modal filters (the labels of the last row on the horizontal axis) of ± 8 , ± 12 , ± 16 , ± 20 and ± 32 , respectively.

Supplementary Notes 7: Demonstration of the tilt angle of the Poynting vector versus light axis

In fact, the Laguerre-Gaussian modes as the solution of the Helmholtz equation under paraxial approximation, are conceived as a standard optical vortex beam, which carries

well-defined OAM. In the cylindrical coordinate (r, φ, z) , the linear momentum density, i.e., the Poynting vector components can be given by [S4, S5],

$$s_r = \frac{\omega k r z}{(z_R^2 + z^2)} |u|^2, s_\varphi = 0, s_z = \omega k |u|^2 \quad (\text{S21})$$

where ω and k are the angular frequency and the wave number of the light, respectively, and z_R is the Rayleigh range of the Gaussian beam. For a well-collimated beam, $s_r \approx 0$ and s_φ / s_z gives the tilt angle between the Poynting vector versus the beam axis to be l / kr . It's clear that for the OAM light field, the Poynting vector is not coincide with the beam propagation direction anymore.

Supplementary Notes 8: General method to choose proper optical modal filters for probing

The principle of choosing the modal filter severely depends on the magnitude of outputted on-axis light intensity. Namely, the higher the output on-axis intensity, the better the probing sensitivity. For illustration, we select E_2 field (see the field distributions in Figs. S1(a) and (e) as well as S4(f)) as an example to illustrate our selection criteria. We first simulate a set of optical modal filter $\Phi_i = E_{0,\pm l}$ from ± 1 to ± 10 orders and calculate the on-axis intensity when projecting them onto the incident E_2 field. The results are displayed in Fig. S8. We can see that except for ± 4 and ± 8 -order optical modal filters, the on-axis intensity for other cases are all null. (see the center of the red cross mark) That is, we just need to choose the optical modal filter with OAM indices consistent with phase-conjugate OAM light fields used to create E_N . In order to further improve the probing sensitivity, it is more judicious to choose a modal filter meeting higher SNR. We can measure the SNRs in turn and compare the magnitude of $|l|/\sqrt{SNR}$ when uploading the selected modal filters (± 4 and ± 8 -orders). The larger the value of $|l|/\sqrt{SNR}$, the higher the detection sensitivity. To summarize, the general method to choose optical modal filters can be divided as two steps: First, to find OAM indices of phase-conjugate OAM light fields within E_N ; second, to select the OAM

indices with the largest value of $|l|/\sqrt{SNR}$ in these candidates for high-sensitive probing.

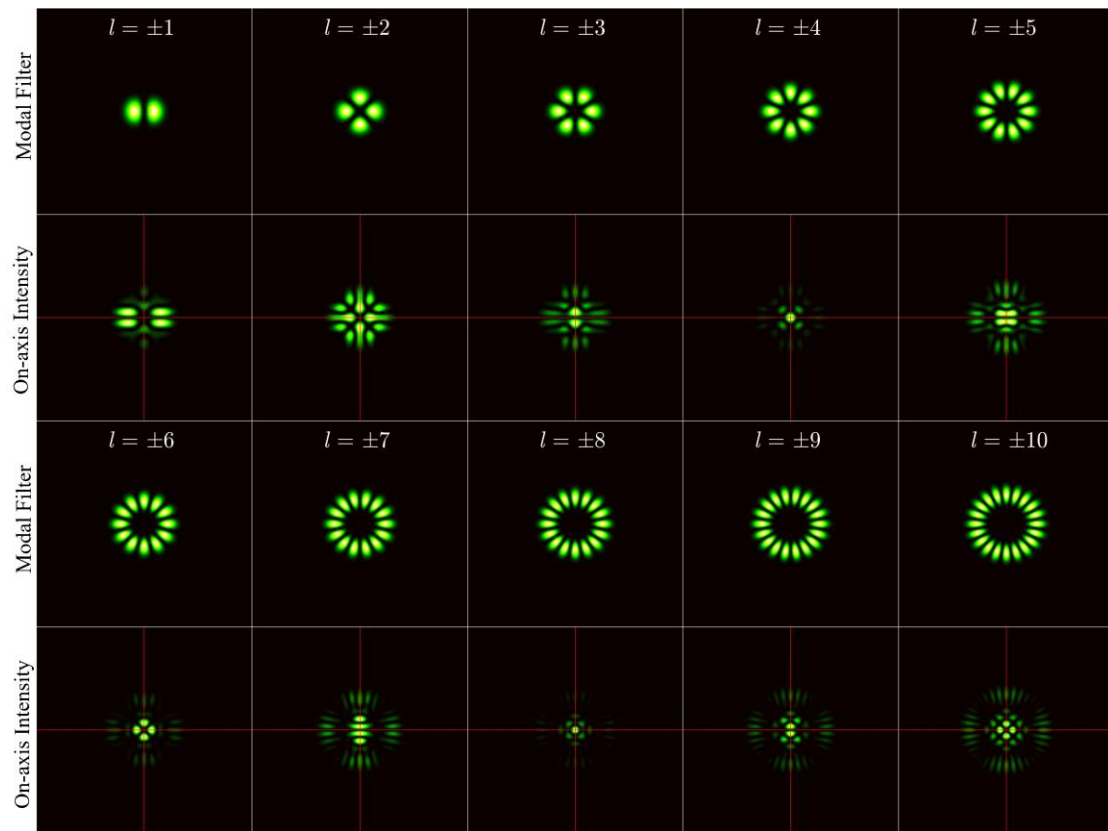


Figure S8 A general method to choose proper optical modal filters. The first and third rows represent the uploaded optical modal filters on SLM1 and SLM2, whereas the second and last rows give the corresponding on-axis intensity distributions (see only the central intensity of red cross mark). Here, E_2 is selected as the emitted light field as an example for illustration.

References

- [S1] Flamm, D. *et al.* Mode analysis with a spatial light modulator as a correlation filter. *Opt. Lett.* **37**, 2478–2480 (2012).
- [S2] Flamm, D. *et al.* All-digital holographic tool for mode excitation and analysis in optical fibers. *J. Lightwave Technol.* **31**, 1023–1032 (2013).
- [S3] Fang, L. *et al.* Sharing a common origin between the rotational and linear Doppler effects. *Laser Photonics Rev.* **11**, 1700183 (2017).
- [S4] Padgett M. J. *et al.* The Poynting vector in Laguerre-Gaussian laser modes. *Opt. Commun.* **121**, 36–40 (1995).

- [S5] Leach, J. *et al.* Direct measurement of the skew angle of the Poynting vector in a helically phased beam. *Opt. Express* **14**, 11919–11924 (2006).
- [S6] Boll, S *et al.* Suppression of acoustic noise in speech using spectral subtraction. *IEEE Trans. Acoust., Speech, Signal Process.* **27**, 113–120 (1979).
- [S7] Zhang, W. H. *et al.* Free-space remote sensing of rotation at the photon-counting level. *Phys. Rev. Appl.* **10**, 044014 (2018).
- [S8] Zhang, W. H. *et al.* Quantum remote sensing of the angular rotation of structured objects. *Phys. Rev. A* **100**, 043832 (2019).